OPEN ACCESS

UNIVERSITY OF DUNDEE

University of Dundee

Seasonal evolution of the Yellow Sea Cold Water Mass and its interactions with ambient hydrodynamic system

Li, Jianchao; Li, Guangxue; Xu, Jishang; Dong, Ping; Qiao, Lulu; Liu, Shidong; Sun, Pingkuo; Fan, Zhisong

Published in:
Journal of Geophysical Research: Oceans

DOI:
10.1002/2016JC012186

Publication date:
2016

Document Version
Final published version

Link to publication in Discovery Research Portal

Citation for published version (APA):
Li, J., Li, G., Xu, J., Dong, P., Qiao, L., Liu, S., ... Fan, Z. (2016). Seasonal evolution of the Yellow Sea Cold Water Mass and its interactions with ambient hydrodynamic system. Journal of Geophysical Research: Oceans , 121(9), 6779-6792. DOI: 10.1002/2016JC012186

General rights
Copyright and moral rights for the publications made accessible in Discovery Research Portal are retained by the authors and/or other copyright owners and it is a condition of accessing publications that users recognise and abide by the legal requirements associated with these rights.

- Users may download and print one copy of any publication from Discovery Research Portal for the purpose of private study or research.
- You may not further distribute the material or use it for any profit-making activity or commercial gain.
- You may freely distribute the URL identifying the publication in the public portal.

Take down policy
If you believe that this document breaches copyright please contact us providing details, and we will remove access to the work immediately and investigate your claim.

AGU PUBLICATIONS

JGR

Journal of Geophysical Research: Oceans

RESEARCH ARTICLE

10.1002/2016JC012186

Key Points:
- The evolution of the YSCWM hydrodynamic system in 1 year was measured
- Large current shear, driven mainly by NIO, developed in concert with the growth of the YSCWM
- The YSCWM shrank during the fortnightly spring tide in autumn

Supporting Information:
- Supporting Information S1

Correspondence to:
G. X. Li,
estuary@ouc.edu.cn

Citation:
Li, J., G. Li, J. Xu, P. Dong, L. Qiao, S. Liu, P. Sun, and Z. Fan (2016), Seasonal evolution of the Yellow Sea Cold Water Mass and its interactions with ambient hydrodynamic system, *J. Geophys. Res. Oceans*, *121*, doi:10.1002/2016JC012186.

Received 27 JUL 2016
Accepted 22 AUG 2016
Accepted article online 29 AUG 2016

© 2016. American Geophysical Union. All Rights Reserved.

Seasonal evolution of the Yellow Sea Cold Water Mass and its interactions with ambient hydrodynamic system

Jianchao Li[1,2], Guangxue Li[2,3], Jishang Xu[2,3], Ping Dong[2,4], Lulu Qiao[2,3], Shidong Liu[2,3], Pingkuo Sun[2,3], and Zhisong Fan[5]

[1]Fisheries College, Ocean University of China, Qingdao, China, [2]Key Lab of Submarine Sciences and Prospecting Techniques, MOE, Ocean University of China, Qingdao, China, [3]College of Marine Geosciences, Ocean University of China, Qingdao, China, [4]School of Science and Engineering, University of Dundee, Dundee, UK, [5]College of Physical and Environmental Oceanography, Ocean University of China, Qingdao, China

Abstract The Yellow Sea Cold Water Mass (YSCWM) is an important component of the hydrodynamic system in the South Yellow Sea (SYS). However, its intricate interactions with the ambient flows over long time scales are not fully understood. This paper presents the analysis of the data set obtained from a seabed-mounted Acoustic Doppler Current Profiler (ADCP) deployed for nearly 1 year in the western SYS. It allowed us to study the evolution of YSCWM, including the seasonal changes of tidal currents, near-inertial oscillations (NIOs), and the wind-driven currents due to typhoons and winter storms. Strong NIOs were found near the bottom of mixed layer and in the pycnocline with nearly opposite current directions, with maximum velocity of nearly 20 $cm \cdot s^{-1}$ in summer. The YSCWM can also inhibit the direct downward energy transport in the water column due to typhoons. Conversely, the hydrodynamic system also feeds back to influence the change of YSCWM. A large current shear (S) of 20 $cm \cdot s^{-1} \cdot m^{-1}$ is generated near the top of pycnocline. Generally, the intensity and depth of the pycnocline determine S's magnitude and vertical location, respectively. Based on the monthly averaged density profile data, the Richardson number and wavelet analysis, the NIOs are considered to be capable of inducing predominant shear instability around the pycnocline. However, the NIOs are not strong enough to influence the lower YSCWM. In addition, in autumn, each fortnightly spring tide corresponds with a bottom temperature increase of nearly 2°C, indicating that tidal currents are the leading hydrodynamic driving force to decline the YSCWM.

1. Introduction

The South Yellow Sea (SYS) is a shallow, semienclosed sea bounded by the Chinese coast and Korean peninsula and transected down its primary axis by a deep North to South trough. It is divided from the North Yellow Sea by a narrowing across a line between Chengshanjiao on the Shandong Peninsula and Changsangot on the Korean Peninsula (Figure 1). A unique hydrological phenomenon, which is seasonally present in the SYS, is the Yellow Sea Cold Water Mass (YSCWM). Generally bordered by the 10°C isotherm and present in summer, the YSCWM spans a wide range above the bottom of central Yellow Sea in summer with relatively low temperature and high salinity below the strong pycnocline [*Lee et al*., 1998; *Lv et al*., 2006; *Xia et al*., 2006; *Hao et al*., 2012; *Oh et al*., 2013]. This stratified summer hydrological condition is quite different from the vertically uniform hydrologic structure present in winter [*Ma et al*., 2006; *Xia et al*., 2006; *Lin et al*., 2011; *Hao et al*., 2012]. During autumn, the sea surface cooling thickens of the mixed layer resulting in the deepening and weakening of the thermocline until the water column becomes isothermal [*Oh et al*., 2013].

A large number of field investigations and observational efforts [*Teague et al*., 1998; *Teague and Jacobs*, 2000; *Tang et al*., 2000, 2004; *Liu et al*., 2007; *Liu et al*., 2008; *Liu et al*., 2009] have shown that the local currents can experience distinct changes with the appearance or disappearance of the YSCWM. The interactions between YSCWM and the ambient hydrodynamic system have also been investigated through theoretical analysis and numerical simulations, both of which indicated that the presence of the YSCWM could cause variations in the diffusion coefficient that influences vertical mixing [*Dai et al*., 2006; *Liu et al*., 2009]. In addition, tidal flows have significant impact on the local current circulation, and their influence is intensified by the interactions with the strong summer stratification [*Lee and Beardsley*, 1999; *Moon et al*., 2009] Further, the boundary of YSCWM is also affected by tidal mixing [*Zhao*, 1986; *Lv et al*., 2010]. Typhoon-

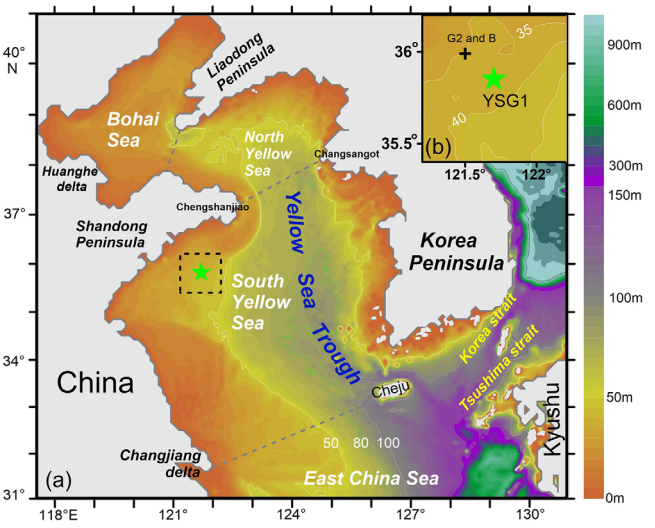

Figure 1. (a) Schematic of the bathymetry of Yellow Sea and the location of YSG1. The background color represents the bathymetry with white, green, and pink contour lines illustrating 50, 80, and 100 m, respectively. The green star indicates the location of YSG1. (b) Detailed information inside the dashed frame in Figure 1a. Besides YSG1 is represented by green star, the black cross shows the location of station G2 and B as supporting information.

driven currents were shown to have a significant impact on the pycnocline, and the strength of the pycnocline is important as its presence inhibits the upward diffusion of suspended particle matters [*Bian et al*., 2010]. As to the current circulation under the combined influence of these unique hydrologic conditions, drifter trajectories in this area have revealed the presence of double counter-rotating current gyres [*Pang et al*., 2004]. Three-dimensional numerical model simulations in this region have also predicted cyclonic (anticlockwise) circulation in the surface layer, with anticyclonic (clockwise) circulation in the near-bed layer (Figure 1) [*Naimie et al*., 2001*; Davies and Xing*, 2006; *Xia et al*., 2006; *Moon et al*., 2009; *Bian et al*., 2013]. However, while these simulations reveal the complexity of the circulation, most numerical results on their effects on the YSCWM are yet to be confirmed by long-term observational data.

The YSCWM was previously thought to originate locally from previous winter water [*Ho et al*., 1959]. But more recent studies have shown that there can also be a southward movement of water from the northern Yellow Sea in summer due to tidal-induced residual currents [*Teague and Jacobs*, 2000*; Zhang et al*., 2007; *Moon et al*., 2009; *Park et al*., 2011; *Wang et al*., 2014]. A complete description of the spatial and temporal evolution of the YSCWM can best be achieved through numerical modeling validated with high-resolution, long-duration time series of local current velocity, temperature and salinity. Fortunately, the evolution of the YSCWM is known to be spatially consistent with the depth of pycnocline being around 10–20 m within the YSCWM despite of the large variation of the seabed topography [*Zhang et al*., 2007]. This means that even with specifically various evolution processes at different locations, the YSCWM as a whole has an integrated evolution pattern. Thus, the long-term measurements at a single observation point can provide valuable information on the evolution histories of the entire YSCWM. Ocean current data obtained using Acoustic Doppler Current Profilers (ADCP) were widely used in previous studies to analyze the regional current evolution and the interactions between hydrodynamic and hydrologic conditions [*Masumoto et al*., 2005; *Byun et al*., 2010; *Alford et al*., 2012; *Chen et al*., 2013]. In addition, according to some previous studies [*MacKinnon and Gregg*, 2012; *Van Haren*, 2000], when supported by relevant density information, the measured current shear structure can be used to infer the mixing processes in the pycnocline. Therefore, the long-term ADCP data can not only be used to explore the relationship between shear current and YSCWM but also the probable mixing processes active during the seasonal evolution of the YSCWM.

Apart from measuring the vertical structure of the flow and the frequency spectrum, profiling current records can be used to study the near-inertial oscillations (NIO) [*Alford et al*., 2012]. The NIOs are characterized by clockwise rotating, near-circular horizontal currents in the northern hemisphere that occur at a frequency near the local inertial frequency [*Chen et al*., 1996]. The strong pycnocline in the SYS during summer offers advantageous conditions for generating NIOs. Several studies on the NIOs in the SYS have been carried out in recent years. *Fang et al*. [1989] first investigated the NIOs in the central SYS by CTD records. *Liu et al*. [2007] and *Tang et al*. [2004] analyzed the NIOs in the SYS in July via rotary spectrum with shipborne and moored ADCP current measurements, respectively. More recently *Liu et al*. [2009] carried out ADCP observations in late September in the western SYS but failed to find any signal from NIOs. However, due to the limited durations of the flow measurements, none of these studies were able to describe the full

Table 1. The ADCP Parameter Settings

	Measurement Period	Water Depth (m)	Vertical Bin Size (m)	Bottom Blind Zone (m)	Surface Blind Zone (m)	Current Ensemble Interval (h)
Stage 1	16 Aug 2012, 20:00 to 25 Oct 2012, 08:00	38	1	3.21	2.29	1/6
Stage 2	25 Nov 2012, 10:00 to 5 Jan 2013, 08:00	38	2	4.20	2.29	1
Stage 3	5 Jan 2013, 12:00 to 27 Mar 2013, 08:00	38	2	4.18	2.29	1
Stage 4	27 Mar 2013, 12:00 to 22 Jul 2013, 08:00	38	2	4.17	2.29	1

evolution cycle of NIOs in the SYS. In addition, it was also clear that the processes responsible for the evolution of the YSCWM had not been completely delineated or understood.

Using a 1 year ADCP observational data set taken near the boundary of YSCWM in the western SYS, this paper investigates the seasonal variation of the YSCWM and its relationship with hydrodynamic system in the research area. This study includes consideration of the effects of tidal currents, NIOs, and storm-related wind-driving currents, and discusses the hydrodynamic factors influencing the vertical hydrological structure of the YSCWM. The long-duration observations of the flow field in the vicinity of the of YSCWM can also be used for calibrating and interpreting large and long-time scale model simulations of the circulation in the SYS and provides the essential hydrodynamic information relevant to ecological, environmental, and agricultural assessments, such as making aquaculture plan in the YSCWM.

2. Data and Methods

2.1. Data

A seabed-mounted ADCP (RDI-300K) observation (named YSG1) was deployed in the western SYS (35.8°N, 121.7°E) at a water depth of 38m from 16 August 2012 to 22 July 2013 (Figure 1). The location of YSG1 was chosen to coincide with the western boundary of the YSCWM (supporting information Figure S1). The upward looking ADCP continuously monitored the currents in the YSCWM for nearly 1 year except for two 3 h gaps for battery changes on 5 January and 27 March of 2013 and a 1 month break from 25 October to 25 November, 2012 to repair the station frame. The data included water depth, flow velocity (eastward, northward and vertical components, *u, v, w*), and bottom water temperature. Each individual ADCP data point recorded the average value of measured currents over a 50 s sampling window. The ADCP measured currents in vertical bins that varied from 1 to 2 m in thickness and the data from the surface bin were discarded due to its low accuracy caused by the presence of bubbles near the surface [*Thorne and Hurther*, 2014]. These parameter settings are shown in Table 1. For consistent comparison with the other three periods, the vertical resolution in period 1 was downgraded in postprocessing from 1 to 2 m by averaging values of every other pair in the two original measurement bins.

In addition to the ADCP data, remote sensing data from the WindSat and TMI/TRMM satellites were gathered for establishing the sea surface temperature (SST) and wind speed and direction (about two samples a day) during the ADCP sampling period. High frequency (hourly) simulated wind data (speed and direction) were obtained from the Weather and Wave Realtime Forecasting System (WRF wind) designed by Prof. Gao Shanhong [*Wu et al*., 2011]. Furthermore, every year there were several voyages of RV Dongfanghong No.2 Ship, which carried out CTD measurements in the area surrounding the location of YSG1. Considering the nearby location and the similar water depth and hydrologic structure within the YSCWM, the temperature profile from the G2 site (121.5°E, 35.99°N, 00:41, 23 June 2013) was used to represent the vertical temperature structure concurrent with the current profile recorded by the ADCP to help interpret the observational data in the present study. In addition, the monthly averaged hydrological data (at a vertical resolution of 5 m) from station B (121.5°E, 36°N), which was closest to YSG1, were used for establishing the background hydrologic conditions. These data were taken from the historical hydrographic database of the First Institute of Oceanography of the State Oceanic Administration (FIO/SOA) of China that has been collected since 1940 [*Yuan et al*., 2013].

2.2. Methods

Typically, tidal currents are the dominant signal affecting the basic hydrodynamic conditions in a shallow sea. Therefore, the analysis made use of a general Matlab package "T_TIDE v1.3 beta," which was created by

Pawlowicz et al. [2002] to perform standard harmonic analysis with nodal corrections and inference to determine the harmonic constants of each tidal constituent. Based on the tidal harmonic constants, the tidal current was reconstructed by T_Tide, and the difference between these tidal currents and the measured current vector was defined as detided current in this paper.

In addition to classical harmonic analysis, the current data were also processed to obtain rotary spectra [*Gonella*, 1972], which could separate the intensity of the clockwise and counterclockwise-rotating current motions of each frequency component. The main aim of rotary spectral analysis was to reveal the existence of NIOs. Then data smoothing in this paper utilized Butterworth filter that was applied twice, once forward and once backward to minimize phase distortion [*Guan et al*., 2014]. Finally, wavelet analysis, using a Morlet wavelet, was employed to determine energy distribution both in the time and frequency domains to indicate the temporal energy distribution at different frequencies. Wavelet analysis has advantages over regular spectrum analysis that only provides a window in the frequency domain.

Vertical variation of currents can greatly influence the various hydrological conditions by inducing or suppressing mixing. For this reason, the vertical shear of the horizontal current velocity, S ($cm{\cdot}s^{-1}{\cdot}m^{-1}$) was determined as follows [*Black and Dickey*, 2008]:

$$S=\sqrt{\left(\frac{\partial u}{\partial z}\right)^2+\left(\frac{\partial v}{\partial z}\right)^2} \tag{1}$$

Here u and v are the eastward and northward velocity components, respectively, and z is the water depth. Therefore, this parameter can effectively represent the extent of current variation.

3. Results

3.1. Overview of the Seasonal Variation of the YSCWM and Hydrodynamic Systems

The time series of bottom temperature measured at YSG1 is shown in Figure 2a. The distribution of the bottom temperature shows clear seasonal characteristics. It experienced intermittent increases since mid-August, and then followed by a continuous decrease until March with a higher rate of change before January. From March, the bottom temperature started to increase again, but at a relatively slow rate until late July. The vertical temperature profile (Figure 2a, vertical red line profile) at the adjacent G2 site demonstrated the existence of the pycnocline in June at water depths from 30 to 23 mab (meter above bottom). According to the measurements of *Liu et al*. [2009], in the western part of YSCWM for water depths shallower than 40 m, in general the temperature is vertically uniform above and below the thermocline in summer. Therefore, the bottom temperature and SST typically represent the temperature of the YSCWM and the surface mixed layer, respectively.

In this study, the temperature difference (TD) between SST (as measured by Remote Sensing Satellites TMI) and bottom temperature (from the ADCP) is taken as an indicator of the YSCWM intensity. Generally, from mid-August when TD was about 15°C, the TD decreases with the gradual decline of SST and intermittent increases of the bottom temperature. By October, the temperature structure becomes vertically homogenous (TD $\sim$ 0), and remains so through April. Beginning in May the TD begins to increase with time until reaching a maximum at the end of July (Figure 2a). Considering the influence of the YSCWM on local current structure, harmonic and rotary spectral analyses for the observed data were carried out for four stages according to the local seasonal boundary (autumn, 17 August to 25 October; winter, 25 November to 28 February; spring, 1 March to 31 May; summer, 1 June to 22 July).

The horizontal current exhibits distinct cyclical variations with both daily and monthly periods. The velocities of the current during different monthly periods were distinct, for instance, the velocity was generally about 50 $cm{\cdot}s^{-1}$ around 1 April but less than 20 $cm{\cdot}s^{-1}$ around 12 March (Figure 2b). The vertical distribution of the current was basically uniform from October to April, but inhomogeneous during the other months.

By comparison, the vertical current, w, with speeds around 1 $cm{\cdot}s^{-1}$ (Figure 2c), is much smaller than the horizontal flow. However, its vertical structure also varies considerably over the year. Similar to horizontal current, the vertical current, w, is relatively uniform throughout the water column from October to April. Starting in May, w begins to increase in the upper part of water column and the depth range of large

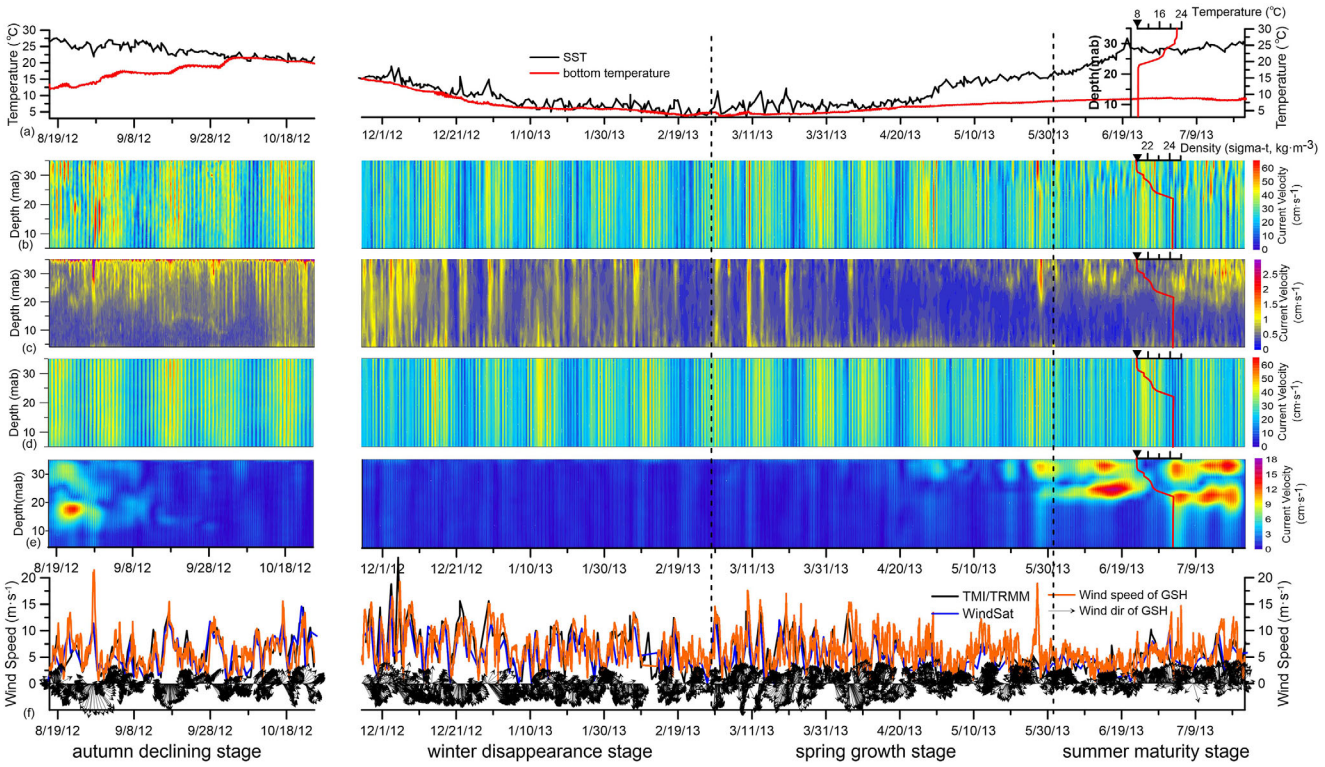

Figure 2. Time series of the ADCP and wind data at the YSG1 site with the gap representing the measurement interruption. The dashed vertical lines separate each stage. The rows from top to bottom are (a) SST and bottom temperature (°C), (b) horizontal current velocity (cm·s^{-1}), (c) absolute value of 6 h averaged vertical current velocity (cm·s^{-1}), (d) predicted tidal current velocity from harmonic analysis (cm·s^{-1}), (e) Butterworth-filtered NIO in the frequency band from 1.1232–1.1952 cpd, and (f) wind speed (m·s^{-1}) and direction from WRF wind field, TMI and Windsat. The profile in red line shows the (a) temperature and (b–e) density profile at G2 from the cruise of RV Dongfanghong No.2 on 23 June. The depth unit "mab" represents "meters above the bottom."

w expands downward with time until finally being nearly uniform by October. In addition, the vertical and horizontal current velocities usually increase markedly when there are rapid increases of wind, such as on 29 August 2012 and 27 May 2013 (Figure 2f). The detailed seasonal current evolution will be discussed in sections 3.2–3.4.

Harmonic analysis is carried out to gain the local tidal current conditions. Define W_X as the maximum velocity of tidal component X, which also represents the length of major axis of the tidal ellipse for tidal component X. Then based upon the value of $(W_{K1} + W_{O1})/W_{M2}$, which is less than 0.5 in all four seasons, the local tidal current is dominated by regular semidiurnal tidal currents. However, the vertical distributions of the tidal currents are not uniform over the four seasons, which is especially pronounced for diurnal tidal current components, O_1 and K_1. Except in winter, the O_1 and K_1 components vary in the direction of their main axis, the initial phase and rotation directions with depth. This variation is particularly evident in summer (supporting information Figure S2). From the time series of the extracted tidal currents (Figure 2d), it is clear that, in addition to the diurnal and semidiurnal tidal components, local tidal currents also have a clear fortnightly period. During the fortnightly spring tide, the horizontal tidal current velocity can exceed 50 cm·s^{-1}, while it only reaches 20 cm·s^{-1} for the fortnightly neap tide. Comparing to the original current velocity signal (Figure 2b), it is clear that the tidal current is the dominant hydrodynamic component in the research area.

An additional component of the flow arises from near-inertial oscillations. The local inertial period is determined by:

$$T = 2\pi/(2\Omega \sin \varphi) \tag{2}$$

where $\Omega = 7.292 \times 10^{-5}$ rad·s^{-1} is the rotation rate of earth and ϕ is the latitude [*Talley et al.*, 2008]. The local inertial period at YSG1 is 20.49 h with a corresponding inertial frequency, *f*, of 1.17 cpd, which is fairly close to the frequency of a high energy signal (1.15 cpd) in clockwise rotary spectrum in spring, summer

and autumn (supporting information Figure S3). Considering the frequency, motion pattern and the position in the water column, this high energy signal is considered to be NIO.

To further analyze the vertical distribution of the local NIO, the *u* and *v* components of the signal with strongest NIO amplitude (1.1232–1.1952 cpd, based on supporting information Figure S3) was extracted by Butterworth filter as described in section 2.2 and its velocity distribution is shown in Figure 2e. There are clearly two locations with strong NIO in the water column, separated by a low-velocity layer in the middle. Compared to the density profile from G2 site at that time, the upper part resides mainly in the upper mixed layer and the lower part is primarily within the pycnocline. The maximum velocity of the NIO is nearly 20 cm·s^{-1}. The seasonal evolution of NIO will be discussed in the following section.

The discontinuity in the NIO velocity signal corresponds with the depth of upper part of pycnocline. The NIO intensifies with the maturity of YSCWM in summer and declines in concert with the disappearing of YSCWM in autumn. The branch of the NIO below the pycnocline generally occurs around 20 mab depth in summer and descends to nearly 15 mab depth by 8 September, after which the NIO weakens. Based on the previous research [*Shearman*, 2005], the depth of NIO discontinuity and its seasonal variation likely indicates the depth and evolution of upper mixed layer.

Based on seasonal changes of the YSCWM shown in the measurements and previous work, the general current evolution in western SYS can be divided into four seasonal stages, which are named after a specific stage of YSCWM: the winter disappearance stage, the spring growth stage, the summer maturity stage, and the autumn declining stage (Figure 2). Their detailed current evolution will be discussed based upon the order of the evolution of YSCWM.

3.2. Winter Disappearance Stage (Late-October to February)

During the time period when the YSCWM disappears, the local hydrological structure is becoming vertically uniform. At the same time, the current velocity was also nearly vertically homogenous. Among the four stages, the tidal current is most predominant in winter. During this time, strong current events with intensified horizontal and vertical current velocities, like those around 3 December 2012 and 1 January 2013, occur throughout the water column, which was clearly different than during the other three stages. In addition, due to the nearly uniform hydrologic structure, NIOs are very weak or nonexistent in this stage.

Taking the winter storm around 30 December as an example (Figure 3a), one of its impacts was to cause the simultaneous increase of detide current velocity throughout the water column to more than 20 cm·s^{-1} (Figure 3b). This high speed current lasted typically for about 1 day from 12 A.M. 29 December, while the strong northwest wind lasted longer for about 2 days. Previous research has demonstrated that the Yellow Sea Coastal Current (YSCC) can be intensified by the actions of winter storms [*Moon et al*., 2009]. Further,

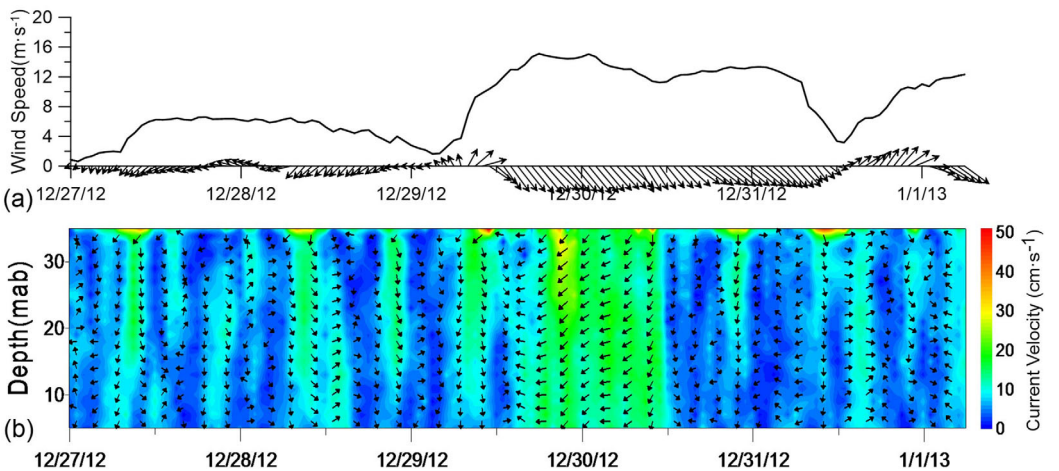

Figure 3. The wind forcing during passage of a winter storm and the distribution of the detide current. (a) Wind speed (m·s^{-1}) and direction (arrow) at the YSG1 site from the WRF wind. (b) Detide current velocity (cm·s^{-1}, color) and horizontal current direction (upward arrow denotes currents in the northward direction).

the change in the direction of the YSCC during the storm events may represent an anticlockwise shift in the route of YSCC driven by a strong, continuous northwesterly wind.

3.3. Spring Growth Stage (March–May)

In this stage, both the SST and bottom temperature start to show increasing trends and the current evolution can be divided into two parts by 20 April, which is the start of the increasing TD. In the first part, with vertically similar temperature structure, the current condition is similar to that in winter when vertical current structure was still relatively homogenous. However, significant horizontal and vertical current variations existed throughout the water column. However, the vertical current velocity already has developed a decreasing trend with time. And NIOs have not yet appeared. After 20 April, the horizontal current starts to become inhomogeneous from upper part of the water column that progresses downward with time. The appearance of NIOs above 25 mab is the main factor contributing to this phenomenon. The velocity of the NIOs is mostly lower than 9 cm s^{-1} and develops in the upper part of the water column except during the strong wind incident on 27 May. At the same time, relatively large vertical currents ($>$1 cm s^{-1}) start to concentrate in the upper water column and begin to expand downward from about 5 to 20 mab. Since then, the pattern of current response to the strong wind is very different from that in the winter disappearance stage. Like on 27 May, it can be clearly seen that the intensification of the vertical currents is primarily restricted to the upper part rather than the whole water column. With the major increase of NIOs above 20 mab, the horizontal current does not synchronously vary over the whole water column.

3.4. Summer Maturity Stage (June to Mid-August)

During the maturity stage, the large TD represents the booming of YSCWM. Under this condition, the vertical variations of horizontal currents are most developed of all four stages. The depth ranges of the horizontal current variation and the large vertical current ($>$1 cm s^{-1}) in the upper water column both slightly deepen from about 22–18 mab during this stage. Below this depth, the vertical structure of the horizontal current is relatively uniform and the vertical current is notably weakened. Concurrently, NIOs with maximum velocities of nearly 20 cm s^{-1} occur and represent the strongest NIOs present among the four stages. As clearly apparent in velocity distribution, two main parts of strong NIOs currents exist in the water column separated by a low-velocity layer whose depth generally varies from 25 to 28 mab. Compared to the NIO during the spring growth stage, in addition to the increased velocity, the other main difference is the intensified NIOs existing in the lower part.

Comparison to the temperature profile at G2 shows that the upper part of NIOs mainly exists in the lower part of upper mixed layer, while the lower part of NIOs corresponded to the depth of pycnocline. In addition to clockwise rotation of current direction, the most dramatic characteristics of the NIOs in this stage are the oppositely directed currents in the two parts of the NIOs (Figure 4). This leads to intense current shear across the low NIO velocity layer as well as enhanced current structure variations in the vertical. In addition, the largest *w* usually occurs at this layer, which indicates a relatively strong vertical disturbance.

3.5. Autumn Declining Stage (Late-August to Mid-October)

In late August when the YSCWM declines, current structure in the water column generally evolves from a highly structured condition toward vertical uniformity as the TD decreases. In this process, the amplitude of the NIOs, primarily causing the vertical nonuniformity, begins to decline. So much so that by 13 September,

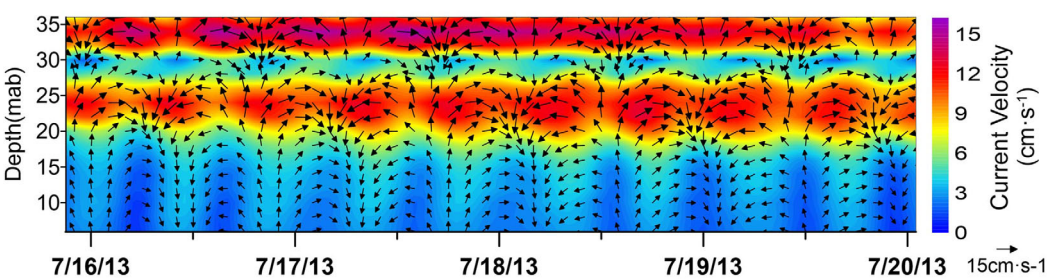

Figure 4. Temporal distribution of the velocity field of the extracted NIOs at the time of large velocity from Figure 2e. The color and arrow represent the speed and velocity of NIOs, respectively.

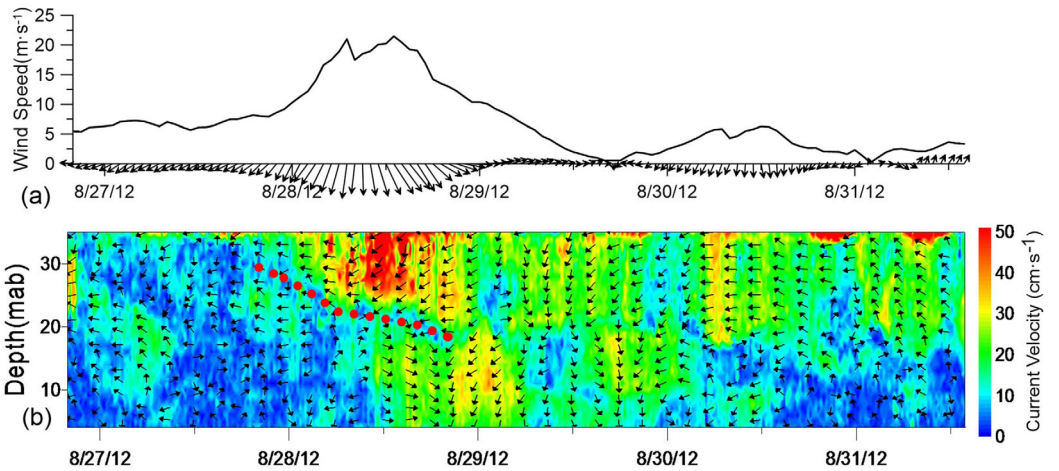

Figure 5. The wind forcing during the passage of a typhoon and the detide current distributions. (a) Wind speed ($m \cdot s^{-1}$) and direction (arrow) at YSG1 from the WRF wind data set. (b) Detide current velocity ($cm \cdot s^{-1}$, color) and horizontal current direction (an upward arrow denotes the northward direction).

the NIOs are too weak to influence the current structure. Looking at the temporal evolution of the NIOs velocities from spring to autumn, its pattern evolves from having stronger velocities in its upper part in spring to a summer state with similar velocities in both parts to a final state in autumn where the velocities are stronger in the lower part. The depth of the upper region of relatively high vertical velocity (>1 $cm \cdot s^{-1}$) and the low NIO velocity layer has a similar downward descent as the TD is decreasing. After 3 October, when the temperature structure becomes vertically homogenous, the horizontal and vertical current structures are uniform throughout the water column.

Due to the presence of the YSCWM, typhoon wind forcing could not generate currents with vertically uniform direction (Figure 5b), even though the wind speeds are larger than those of winter storms (Figure 5a). There is an apparent internal low-velocity layer with different current directions in its two sides that deepening during the passage of a typhoon. This occurred even though the speed of the typhoon-driven detide currents exceeded 50 $cm \cdot s^{-1}$, roughly 2.5 times stronger than those generated by a winter storm (20 $cm \cdot s^{-1}$). However, the descending of the range of the upper region of intense typhoon currents still demonstrated the deepening of the upper mixed layer result from typhoon as indicated by the previous research [*Black and Dickey*, 2008]. In addition, after roughly a 12 h delay from the response of the upper layer currents, the detide currents in the lower water column began to intensify. This relatively high-speed and vertically inhomogeneous current structure persisted for roughly 2 days after the passage of the typhoon.

4. Discussions

4.1. Current Shear in the YSCWM Evolution

In order to achieve a fuller understanding of the interactions between the YSCWM and ambient flows, the monthly averaged hydrological data (Figure 6a) have been linearly interpolated temporally and vertically to match the in ADCP ensemble intervals. This allows for a direct comparison between the interpolated hydrological data and the ADCP data. The specific time frame for the 12 monthly averaged data was chosen as close as possible to the measurement of SST and bottom temperature data from ADCP, and then the data were used to calculated the density, ρ (Figure 6b), and buoyancy frequency, N^2 (Figure 6c). The depth of pycnocline (thickness of the upper mixed layer) was determined by the location of the largest N^2. The evolutions of the vertical temperature and density during 1 year clearly illustrate that the pycnocline forms and begins to descend from May, and its depth generally remains at around 20–28 mab in summer maturity stage, which basically corresponds with the density profile from the G2 station. In the autumn decline stage, the upper mixed layer deepens as the TD decreases until it reaches a vertically uniform hydrological structure in October. During the YSCWM evolution, the strength of pycnocline, varying directly with the TD, indicates the intensity of YSCWM.

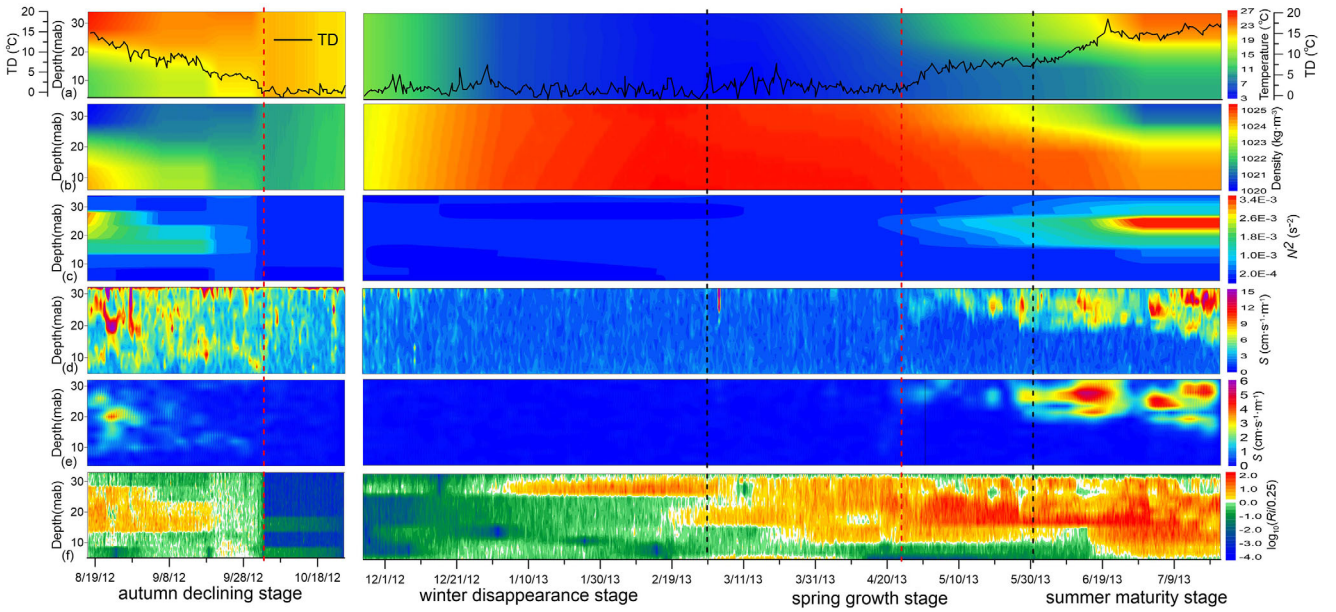

Figure 6. Time series of hydrological features and S in the water column with the gap representing the measurement interruption. The dashed black lines separate each stage. The dashed red lines represent the end and start of the YSCWM. The rows from top to bottom are (a) temperature (color, °C), TD (black line, °C). (b) Density (kg·m^{-3}). (c) Buoyancy frequencies N^2 (s^{-2}). (d) S (cm·s^{-1}·m^{-1}) of the original horizontal current (illustrating largest value in every 12 h). (e) S (cm·s^{-1}·m^{-1}) of the filtered NIO from Figure 2e. (f) $\log_{10}$(Ri/0.25), the normalized Richardson number (Ri).

The *S* values (Figure 6d) of the original current represent the integrated impacts of the YSCWM on tidal currents, NIO and wind-driven currents. In order to remove the periodic changes and highlight the trend, the large envelope curve (maximum value of every 12 h) of *S* was used for further analysis. In the period of homogeneous temperature structure from October to April, the vertical current structure is stable with *S* lower than 2.5 cm·s^{-1}·m^{-1}. However, in the presence of the YSCWM, large *S* develops in the water column. Generally, the depth of the relatively large *S* is near the upper part of the pycnocline and its intensity scales with TD. With the appearance of YSCWM in April, strong variations of the current structure occur in the upper part of water column. With the maturity of YSCWM, the region of strong *S* (>8 cm·s^{-1}·m^{-1}) gradually expands downward to about 15 mab indicating the expansion of the vertical current variability due to the larger effects of a maturing YSCWM. The *S* around the pycnocline also peaks in summer. During the autumn decline stage, the region of relative high *S* descends with the depth variation of pycnocline and its value also decreases as the TD weakens, reflecting the trend toward vertically uniform current structure. Below the upper high *S* region within the YSCWM, the current structure was stable and vertically homogenous with low *S* during both the spring growth and summer maturity stages (Figure 6d). The *S* of NIO in Figure 2e is also calculated (Figure 6e). Large *S* from NIO (nearly 6 cm·s^{-1}·m^{-1}) is generated around the low-velocity NIO layer. In the upper high *S* region, the depth of largest *S* corresponds with the depth of largest *S* from NIOs (Figure 6f) and largest *w* (Figure 2c). Because of the considerable speed and the oppositely directed flow between the two sides of pycnocline, the NIOs generate remarkable *S* and are considered to be the primary factor leading to the variation of vertical current structure during the existence of the YSCWM. To confirm this, wavelet analysis was applied to the *u* component of *S* in the upper region with larger *S* from March to July (Figure 7). The results confirm the dominating influence of the NIOs in the distribution of *S*, with secondary effects arising from oscillations at the diurnal period. Despite their larger current velocity, semidiurnal tidal currents do not induce significant *S*.

Previous studies [*Van Haren*, 2000; *MacKinnon and Gregg*, 2012] have shown that the current shear pattern can indicate the mixing status of water because mixing is often induced when strong current shear is present. Therefore, in contrast to the hydrologic data (Figures 6a–6c), the observed intense *S* in the upper part of the water column (Figure 6d) implies a relatively unstable state especially around the pycnocline. According to the previous research [*Black and Dickey*, 2008; *Guan et al*., 2014], shear instability occurs when the gradient Richardson number (*Ri*) is lower than a critical threshold value (nominally 0.25). *Ri* is computed here as N^2/S^2. For simple visualization, the normalized *Ri* defined as $\log_{10}(|Ri/0.25|)$ used with

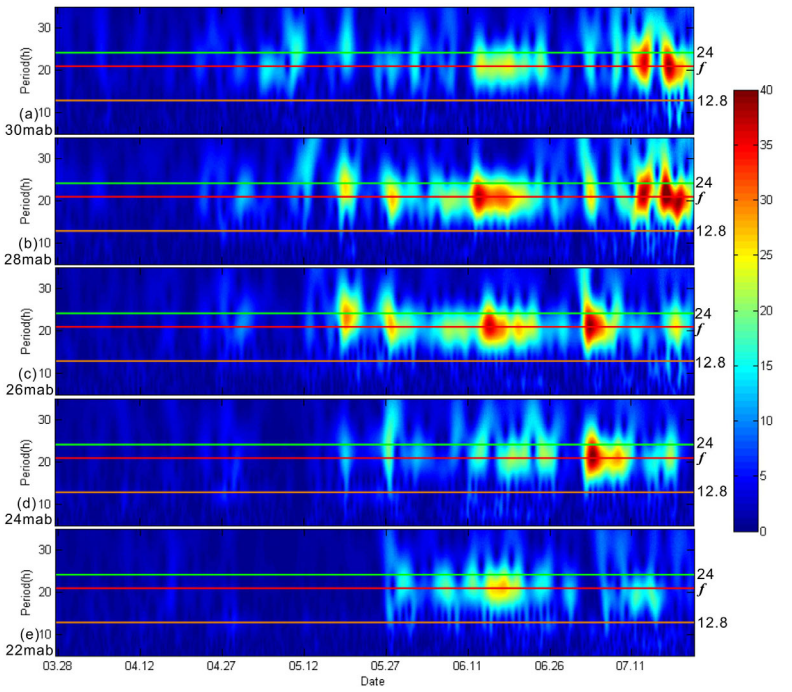

Figure 7. Time series of wavelet power spectra (color: $cm^2 \cdot s^{-2}$) of the components of *S* from the original horizontal current at (a) 30 mab, (b) 28mab, (c) 26mab, (d) 24mab, and (e) 22mab. The diurnal period, inertial period, and period of M_2 are indicated by horizontal green, red, and orange lines, respectively.

$\log_{10}(|Ri/0.25|) > 0$ represents a vertically stratified and $\log_{10}(|Ri/0.25|) < 0$ representing current shear that is strong enough to overcome the stratification and induce turbulent mixing. Although these values are not based on real-time hydrological measurements, the results can still shed useful light on shear instability and associated mixing processes.

The normalized *Ri* presented in Figure 6e shows that during the maturity stage of the YSCWM, most of the water column is relatively stable except near the surface and bottom. However, shear instability may exist in the layer of largest *S*, which coincides with the depth of the low-velocity NIO layer and largest *w*. From the analysis above, the NIOs are thought to be the predominant component responsible for the strong *S* when the YSCWM is present. Therefore, the NIO is supposed to account for the shear instability and possible mixing near the pycnocline. In this way, the necessary mixing in the ocean may be produced, which has important implications for the local environmental ecology. However, according to the variation of bottom temperature (Figure 2a) and *Ni* (Figure 6f), the lower part of water column within the YSCWM may still be relatively stable. Consequently, the bottom temperature did not show notable fluctuations even when the NIOs were most intense during the maturity stage of the YSCWM. This suggests that the strong shear instability generated by the NIOs is restricted primarily to the vicinity of the upper part of the pycnocline and the influence of NIOs is incapable of reaching the bottom of the YSCWM.

In addition to the action of NIOs, it was shown in the preceding sections that the passage of a typhoon also has significant impact on the YSCWM. The *Ri* distribution during the passage of a typhoon (Figure 6f) shows an obvious increase in the shear instability and the possible deepening of the mixed layer. According to previous research [*Black and Dickey*, 2008], typhoons can greatly deepen the upper mixed layer and reduce the stratification so that it is much weaker than normal. As a result, the structure of the YSCWM can be significantly disturbed by typhoon-driven currents and it correspondingly increase the bottom temperature (about 2°C during this typhoon (Figure 2a around 29 August)).

4.2. Decline of YSCWM Driven by Tidal Current

Tidal currents, being the dominant local hydrodynamic factor, are expected to have significant impact on the evolution of the YSCWM. Even though their influence is not apparent during the spring growth and summer maturity stages, the tidal current is critical factor during the autumn decline stage (Figure 8). It can

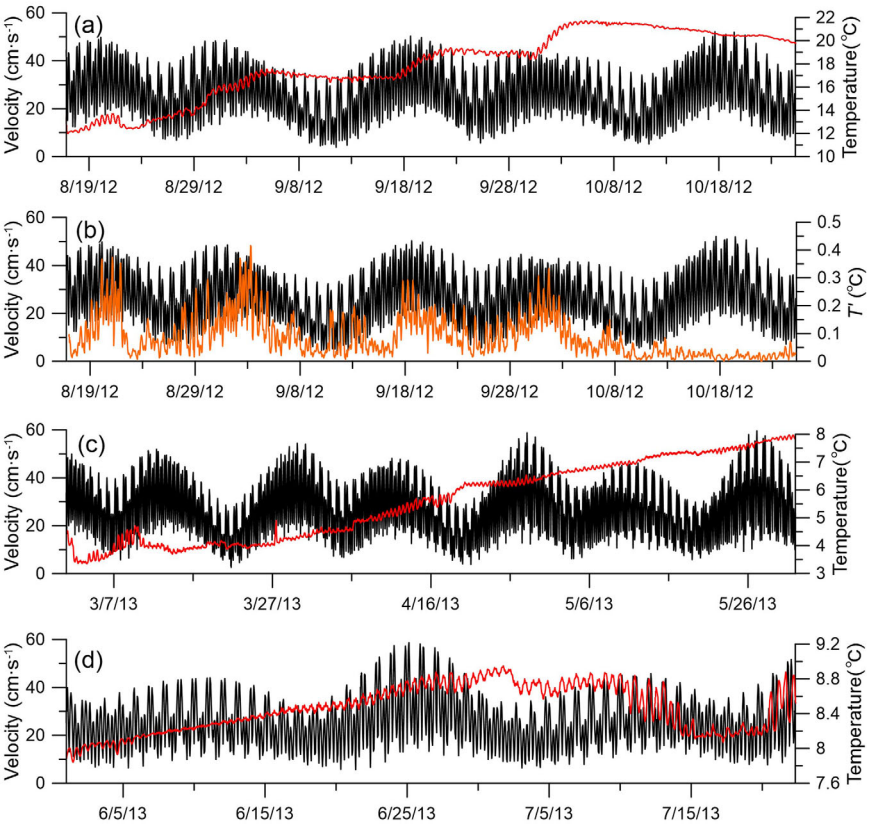

Figure 8. Time series of the barotropic tidal current speed (cm·s^{-1}, vertically averaged data) and bottom temperature (°C) and temperature variation parameter, T' (°C). (a) Autumn, (b) autumn, (c) spring, and (d) summer. The black, red, and orange lines represent the barotropic tidal current speed, the bottom temperature, and T' (°C), respectively.

be clearly seen that before the temperature becomes vertically uniform, during every fortnightly spring tide, the bottom temperature experiences a dramatic increase of approximately 2°C (Figure 8a). To study this in detail, we define the bottom temperature variation parameter, T', as:

$$T' = sqrt(((t-t_{2-})^2+(t-t_{1-})^2+(t-t_{1+})^2+(t-t_{2+})^2)/4) \quad (3)$$

Here t_{2-}, t_{1-}, t_{1+}, and t_{2+} are temperature values at time intervals before (−) and after (+) time t. This parameter serves to indicate the degree of variation in the temperature, and can directly highlight that the strong barotropic tidal currents result in large bottom temperature variations when the YSCWM is declining (Figure 8b). After the TD nearly disappears in October, the fortnightly spring tide no longer causes this regular fluctuation of the bottom temperature. Due to the critical observation position near the boundary of the YSCWM, this result provides adequate proof that the fluctuations in bottom temperature are clearly influenced by the fortnightly spring tide during the autumn decline stage of the YSCWM. Furthermore, the YSCWM temperature generally increases when the tidal current direction rotates anticlockwise from about 315° to 135° and a high tidal level (Figure 9).

With respect to the question of which hydrodynamic mechanism is responsible for this warming process, several possibilities exist. One is that because the fortnightly spring tide has stronger tidal currents, it could trigger stronger vertical tidal mixing. In the autumn decline stage, the decrease of the SST is associated with a weakening of the thermocline. As a result, the strong tidal mixing may enhance vertical heat exchange between the water below and above the thermocline and thereby increase the bottom temperature. This mechanism appears to be supported by the fact that the upper high w is deepening as the result of fortnightly spring tide (Figures 2c and 2d), which is correlated with the downward expansion of the upper mixed layer during fortnightly spring tides.

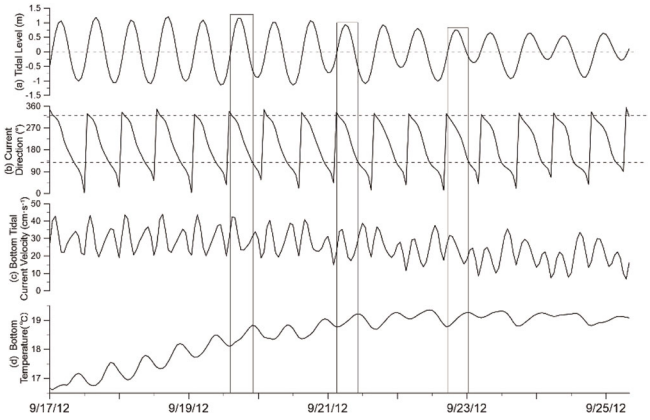

Figure 9. Detailed time series of temperature and current during the autumn decline stage. (a) Tidal level (m) from harmonic analysis (with averaged water depth removed), (b) bottom tidal current direction (°), (c) bottom tidal current velocity ($cm \cdot s^{-1}$), and (d) bottom temperature (°C). The three rectangles represent the time frame of three warming events and the dashed horizontal lines represent the mean tidal level in Figure 9a and the direction of the tidal current at the beginning and ending time of the warming events in Figure 9b, respectively.

An alternate but equally plausible explanation can be found in the strong horizontal advection that occurs during the fortnightly spring tides. These large spring tidal currents can promote more effective horizontal heat exchange among water masses. Further, the correlation between high water levels and increased bottom temperatures implies a possible mechanism of the rotating movement of water from the warmer coastal zone to the YSCWM under an anticlockwise tidal amphidromic system. Conceptually, every tidal cycle represents one energy exchange event between the warm coastal water and the cold water in the western YSCWM, which warms up the cold water and induces a stepwise decline of the YSCWM, the descent of the upper mixed layer and a decrease in TD that continues until the disappearance of the YSCWM.

More long-term measurements of flow, especially measurements of turbulence and concurrent CTD measurements are clearly required to establish whether vertical mixing or horizontal advection or a mixture of both is the dominant mechanism. Despite of this uncertainty, the observations clearly demonstrate that the decline of YSCWM is an intermittent process instead of a continuous one and that the fortnightly spring tide exerts a critical control on the evolution of the YSCWM. It should be noted that the fortnightly spring tide during summer maturity stage does not result in a bottom temperature increase, suggesting there exists a critical level of stratification that is necessary for the spring tidal current mixing to be able to modify the YWCWM. In other words, the decrease of solar energy input in autumn is the primary cause for the decline of the YSCWM while the fortnightly spring tide provides the driving force to drive the decline through either vertical mixing or a horizontal convection mechanism.

5. Conclusion

A seabed-mounted ADCP observation (YSG1) was placed in the western SYS near the boundary of YSCWM for about one year to investigate the variation of the YSCWM and its relationship with the ambient hydrodynamic system. Owing to its sensitive location for the variation of the YSCWM and with supplementary wind and monthly averaged hydrological data, the variation of the hydrodynamic system as the YSCWM evolves and the hydrodynamic factors influencing that YSCWM evolution can be studied from this site.

According to the measurements, regular semidiurnal tidal currents were the dominant hydrodynamic signal with maximum tidal current velocities exceeding 60 $cm \cdot s^{-1}$ during fortnightly spring tides. The hydrodynamic system showed significant seasonal characteristics that change in concert with the evolution of the YSCWM, mainly because of the variation of the NIOs. In the winter disappearance stage, the hydrologic and hydrodynamic structures are both vertically uniform and the action of winter storms causes vertically homogenous wind-driven currents. When the TD increases beginning in May, the NIOs around the pycnocline generally appear during the YSCWM growth stage. As the YSCWM reaches maturity and the pycnoline stabilizes at about 25 mab, the NIO velocities increase to about 20 $cm \cdot s^{-1}$ with nearly oppositely directed flow in its two parts, one near the bottom mixed layer and the other in the pycnocline. During the decline stage of YSCWM, the TD decreases and the pycnocline descends, so that the depth where the NIOs occur is also descending while the amplitude of the NIOs weakens. During this time, even though the YSCWM is weakened, it is normally still capable of preventing the direct downward transport of energy from the

passage of typhoons which results in an asymmetrical current structure. After October, the YSCWM is no longer present at this measurement site.

The presence of NIOs is influential to YSCWM due to their strong S ($>$ 20 cm·s^{-1}·m^{-1}), which may induce shear instability around the upper part of pycnocline according to Richardson number and w distribution. Generally, the intensity of YSCWM determines the magnitude of S and the pycnocline determines the location of maximum S. However, despite of the intense S, NIOs are still unable to break down the pycnocline and influence the bottom part of YSCWM during summer maturity stage. Tidal currents are also expected to have significant impacts on the evolution of the YSCWM, especially during the autumn decline stage. The intermittent increase of bottom temperature indicates the fortnightly spring tide is the main hydrodynamic cause for the decline of YSCWM. In addition, the passage of typhoons may also help accelerate the decline of the YSCWM.

Even without real-time hydrologic profile data, the seasonal evolution and interaction between the YSCWM and the hydrodynamic system from the long-term observed ADCP data have shed further light on the complex flow and mixing processes affected by the YSCWM.

Acknowledgment

We are grateful to the anonymous reviewers for their inspiring and constructive comments, which are helpful in improving the research. The satellite remote sensing data are available at www.remss.com. The WRF wind data are available online at http://222.195.136.24. The monthly hydrological data are obtained from the historical hydrographic database of the First Institute of Oceanography of the State Oceanic Administration (FIO/SOA) of China. We are very thankful for Shanhong Gao, Dongliang Yuan, and Yao Li for providing the data above. The mooring and field data in this work are collected and managed by Ocean University of China. The processed mooring and field data used to construct figures in this work will be made accessible by requisition through e-mail (estuary@ouc.edu.cn). Any users of this data are required to clearly acknowledge the support of Ocean University of China. This study was supported by China Geological Survey-class II project (grant 121201005000150004), the National Natural Science Foundation of China (grant 41030856, 41406081, and 41275084), and the Project of Taishan Scholar. We also thank the support of the Shared Voyage of National Nature Science Foundation of China.

References

Alford, M. H., M. F. Cronin, and J. M. Klymak (2012), Annual cycle and depth penetration of wind-generated near-inertial internal waves at Ocean Station Papa in the northeast Pacific, *J. Phys. Oceanogr.*, *42*, 889–909, doi:10.1175/JPO-D-11-092.1.

Bian, C., W. Jiang, and R. J. Greatbatch (2013), An exploratory model study of sediment transport sources and deposits in the Bohai Sea, Yellow Sea, and East China Sea, *J. Geophys. Res. Oceans*, *118*, 5908–5923, doi:10.1002/2013JC009116.

Bian, C. W., W. S. Jiang, and D. H. Song (2010), Terrigenous transportation to the Okinawa Trough and the influence of typhoons on suspended sediment concentration, *Cont. Shelf Res.*, *30*, 1189–1199, doi:10.1016/j.csr.2010.03.008.

Black, W. J., and T. D. Dickey (2008), Observations and analyses of upper ocean responses to tropical storms and hurricanes in the vicinity of Bermuda, *J. Geophys. Res.*, *113*, C08009, doi:10.1029/2007JC004358.

Byun, S.-S., J. J. Park, K.-I. Chang, and R. W. Schmitt (2010), Observation of near-inertial wave reflections within the thermostad layer of an anticyclonic mesoscale eddy, *Geophys. Res. Lett.*, *37*, L01606, doi:10.1029/2009GL041601.

Chen, C., R. O. Reid, and W. D. Nowlin (1996), Near-inertial oscillations over the Texas-Louisiana shelf, *J. Geophys. Res.*, *101*(C2), 3509–3524.

Chen, G., H. Xue, D. Wang, and Q. Xie (2013), Observed near-inertial kinetic energy in the northwestern South China Sea, *J. Geophys. Res. Oceans*, *118*, 4965–4977, doi:10.1002/jgrc.20371.

Dai, D., F. Qiao, C. Xia, and K. T. Jung (2006), A numerical study on dynamic mechanisms of seasonal temperature variability in the Yellow Sea, *J. Geophys. Res.*, *111*, C11S05, doi:10.1029/2005JC003253.

Davies, A. M., and J. Xing (2006), Effect of topography and mixing parameterization upon the circulation in cold water domes, *J. Geophys. Res.*, *111*, C03018, doi:10.1029/2005JC003066.

Fang X., Y. Zhang, H. Sun, and J. Ye (1989), An investigation of the properties of low-frequency internal waves in the northeastern China Seas, *Chin. J. Oceanol. Limnol.*, *7*(4), 289–299.

Gonella, J. (1972), A rotary-component method for analyzing meteorological and oceanographic vector time series, *Deep Sea Res. Oceanogr. Abstr.*, *19*, 833–846.

Guan, S., W. Zhao, J. Huthnance, J. Tian, and J. Wang (2014), Observed upper ocean response to typhoon Megi (2010) in the Northern South China Sea, *J. Geophys. Res. Oceans.*, *119*, 3134–3157, doi:10.1002/2013JC009661.

Hao, J., Y. Chen, F. Wang, and P. Lin (2012), Seasonal thermocline in the China Seas and northwestern Pacific Ocean, *J. Geophys. Res.*, *117*, C02022, doi:10.1029/2011JC007246.

Ho, C. P., Y. X. Wang, Z. Y. Lei, and S. Xu (1959), A preliminary study of the formation of Yellow Sea cold mass and its properties, *Oceanol. Limnol. Sin.*, *2*, 11–15.

Lee, S. H., and R. C. Beardsley (1999), Influence of stratification on residual tidal currents in the Yellow Sea, *J. Geophys. Res.*, *104*(C7), 15,679–15,701, doi:10.1029/1999JC900108.

Lee, Y. C., Y. S. Qin, and R. Y. Li (Eds.) (1998), *Yellow Sea Atlas*, 524 pp., Chin. Acad. of Sci., Beijing.

Lin, X., J. Yang, J. Guo, Z. Zhang, Y. Yin, X. Song, and X. Zhang (2011), An asymmetric upwind flow, Yellow Sea Warm Current: 1. New observations in the western Yellow Sea, *J. Geophys. Res.*, *116*, C04026, doi:10.1029/2010JC006513.

Liu, Z. L., D. X. Hu, X. H. Tang, and E. B. Wei (2007), Rotary spectrum analysis of tidal current in the southern Yellow Sea, *Chin. J. Oceanol. Limnol.*, *25*, 286–291.

Liu, Z. L., D. X. Hu, and X. H. Tang (2008), Tidal current observation in the southern Yellow Sea in the summers of 2001 and 2003, *Chin. J. Oceanol. Limnol.*, *2*, 121–129.

Liu, Z. Y., W. Hao, I. D. Lozovatsky, and H. J. S. Fernando (2009), Late summer stratification, internal waves, and turbulence in the Yellow Sea, *J. Mar. Syst.*, *77*, 459–472, doi:10.1016/j.jmarsys.2008.11.001.

Lv, X. G., F. L. Qiao, C. S. Xia, J. R. Zhu, and Y. L. Yuan (2006), Upwelling off Yangtze River estuary in summer, *J. Geophys. Res.*, *111*, C11S08, doi:10.1029/2005JC003250.

Lv, X. G., F. L. Qiao, C. S. Xia, G. S. Wang, and Y. L. Yuan (2010), Upwelling and surface cold patches in the Yellow Sea in summer: Effects of tidal mixing on the vertical circulation, *Cont. Shelf Res.*, *30*, 620–632, doi:10.1016/j.csr.2009.09.002.

Ma, J., F. Qiao, C. Xia, and C. S. Kim (2006), Effects of the Yellow Sea Warm Current on the winter temperature distribution in a numerical model, *J. Geophys. Res.*, *111*, C11S04, doi:10.1029/2005JC003171.

MacKinnon, J. A., and M. C. Gregg (2012), Mixing on the late-summer New England shelf-solibores, shear, and stratification, *J. Phys. Oceanogr.*, *33*, 1476–1492.

Masumoto, Y., H. Hase, Y. Kuroda, H. Matsuura, and K. Takeuchi (2005), Intraseasonal variability in the upper layer currents observed in the eastern equatorial Indian Ocean, *Geophys. Res. Lett.*, *32*, L02607, doi:10.1029/2004GL021896.

Moon, J. H., N. Hirose, and J. H. Yoon (2009), Comparison of wind and tidal contributions to seasonal circulation of the Yellow Sea, *J. Geophys. Res.*, *114*, C08016, doi:10.1029/2009JC005314.
Naimie, C. E., C. A. Blain, and D. R. Lynch (2001), Seasonal mean circulation in the Yellow Sea—A model-generated climatology, *Cont. Shelf Res.*, *21*,667–21,695, doi:10.1016/S0278-4343(00)00102-3.
Oh, K. H., S. Lee, K. M. Song, H. J. Lie, and Y. T. Kim (2013), The temporal and spatial variability of the Yellow Sea Cold Water Mass in the southeastern Yellow Sea, 2009–2011, *Acta Oceanol. Sin.*, 9, 1–10, doi:10.1007/s13131-013-0346-9.
Pang, C. G., J. X. Liang, D. X. Hu, F. Wang, Y. L. Chen, H. Bai, and X. Z. Bai (2004), Surface circulation patterns observed by drifters in the Yellow Sea in summer of 2001, 2002 and 2003, *Chin. J. Oceanol. Limnol.*, *22*, 209–214.
Park, S. H., P. C. Chu, and J. H. Lee (2011), Interannual-to-interdecadal variability of the Yellow Sea cold water mass in 1967–2008: Characteristics and seasonal forcings, *J. Mar. Syst.*, *87*, 177–193, doi:10.1016/j.jmarsys.2011.03.012.
Pawlowicz, R., B. Beardsley, and S. Lentz (2002), Classical tidal harmonic analysis including error estimates in MATLAB using T_TIDE, *Comput. Geosci.*, *28*(8), 929–937, doi:10.1016/S0098-3004(02)00013-4.
Shearman, R. K. (2005), Observations of near-inertial current variability on the New England shelf, *J. Geophys. Res.*, *110*, C02012, doi:10.1029/2004JC002341.
Talley, L. D., G. L. Pickard, W. J. Emery, and J. H. Swift (2008), *Descriptive Physical Oceanography: An Introduction*, Academic, San Diego, Calif.
Tang, X. H., F. Wang, Y. L. Chen, H. Bai, and D. X. Hu (2004), Current observations in the southern Yellow Sea in summer, *Chin. J. Oceanol. Limnol.*, *3*, 217–223.
Tang, Y. X., E. M. Zou, H. J. Lee, and J. H. Lie (2000), Some features of circulation in the southern Yellow Sea, *Acta Oceanol. Sin.*, *22*, 1–16.
Teague, W. J., and G. A. Jacobs (2000), Current observations on the development of the Yellow Sea Warm Current, *J. Geophys. Res.*, *105*(C2), 3401–3411, doi:10.1029/1999JC900301.
Teague, W. J., H. T. Perkins, Z. R. Hallock, and G. A. Jacobs (1998), Current and tide observations in the southern Yellow Sea, *J. Geophys. Res.*, *103*(C12), 27,783–27,793.
Thorne, P. D., and D. Hurther (2014), An overview on the use of backscattered sound for measuring suspended particle size and concentration profiles in non-cohesive inorganic sediment transport studies, *Cont. Shelf Res.*, *73*, 97–118, doi:10.1016/j.csr.2013.10.017.
Van Haren, H. (2000), Properties of vertical current shear across stratification in the North Sea, *J. Mar. Res.*, *58*, 465–491.
Wang, B., N. Hirose, B. Kang, and K. Takayama (2014), Seasonal migration of the Yellow Sea Bottom Cold Water, *J. Geophys. Res. Oceans.*, *119*, 4430–4443, doi:10.1002/2014JC009873.
Wu, D. X., S. H. Gao, Y. M. Wang, and X. E. Chen (2011), *Atlas of Monthly Averaged Wind and Temperature of Bohai and Yellow Sea*, China Ocean Univ. Press, Qingdao, China.
Xia, C., F. Qiao, Y. Yang, J. Ma, and Y. Yuan (2006), Three-dimensional structure of the summertime circulation in the Yellow Sea from a wave-tide-circulation coupled model, *J. Geophys. Res.*, *111*, C11S03, doi:10.1029/2005JC003218.
Yuan, D. L., Y. Li, F. L. Qiao, and W. Zhao (2013), Temperature inversion in the Huanghai Sea bottom cold water in summer, *Acta Oceanol. Sin.*, *32*(3), 42–47, doi:10.1007/s13131-013-0287-3.
Zhang, S. W., Q. Y. Wang, Y. Lu, H. Cui, and Y. L. Yuan (2007), Observation of the seasonal evolution of the Yellow Sea Cold Water Mass in 1996–1998, *Cont. Shelf Res.*, *28*, 442–457, doi:10.1016/j.csr.2007.10.002.
Zhao, B. R. (1986), The fronts of the Huanghai cold water mass (HCWM) induced by tidal mixing, *Chin. J. Oceanol. Limnol.*, *4*(2), 159–170.